

Bayesian spectroscopy on polarization dependent photoluminescence spectra of doubly-split excitons in a Cu₂O thin-crystal sandwiched by MgO substrates

A. Kiridoshi¹, S. Aihara¹, S. Arishima¹, T. Yamashiro¹, M. Mizumaki², K. Iwamitsu^{*,3}, I. Akai⁴

¹ Graduate school of Science and Technology, Kumamoto University, 2-39-1 Kurokami, Chuo-ku, Kumamoto 860-8555, Japan.

² Japan Synchrotron Radiation Research Institute, Sayo, Hyogo 679-5148, Japan.

³ Faculty of Science, Kumamoto University, 2-39-1 Kurokami, Chuo-ku, Kumamoto 860-8555, Japan.

⁴ Institute of Pulsed Power Science, Kumamoto University, 2-39-1 Kurokami, Chuo-ku, Kumamoto 860-8555, Japan.

Key words: Bayesian spectroscopy, exciton, biaxial stress effect, polarization dependence, Cu₂O

* Corresponding author: e-mail iwamitsu@kumamoto-u.ac.jp

By using Bayesian spectroscopy, we studied polarization dependence of photoluminescence (PL) spectra in doubly-split 1S yellow ortho-excitons in a Cu₂O thin-crystal recrystallized in a small gap between paired MgO substrates. In these thin-crystals, biaxial stresses are expected to be involved due to a small lattice mismatch between Cu₂O and MgO. Under a planar-isotropic biaxial stress, the cubic symmetry degrades to the tetragonal one in Cu₂O, and subsequently, the ortho-exciton state splits into two states having different symmetries. Consequently, the resonant PL intensities of the doubly-split ortho-excitons are expected to show different polarization dependencies. To elucidate such biaxial stress effect, we measured polarization dependence of the PL spectra at 4.2 K. Although resonant weak PL bands of the doubly-split exciton states and their intense phonon sidebands co-exist, we succeeded in decomposing to the respective spectral components by the Bayesian spectroscopy with a replica exchange Monte Carlo algorithm. As a result, it was found that the resonant PL band appearing on higher energy side shows hardly polarization dependence, whereas the resonant PL band appearing on lower energy side is further weak and shows noticeable polarization dependence. These results can be explained by the selection rule and polarization dependences on the transition matrix elements of quadrupole transitions of the doubly-split ortho-exciton states, and it clearly shows that the crystal symmetry degrades to D_{4h} by the isotropic biaxial stress involved in the Cu₂O thin-crystals.

Copyright line will be provided by the publisher

1 Introduction Excitonic systems in Cu₂O are promising candidates for excitonic Bose-Einstein condensation (X-BEC) and have been deeply studied having a long history [1]. Recently, Yoshioka *et al.* [2] discovered a “relaxation explosion” phenomenon in a Cu₂O bulk crystal at sub-Kelvin temperatures, and they insisted that it is a direct manifestation for realization of X-BEC. Surely, photo-excited excitons diffuse into low density region, and subsequently, the exciton density usually decreases. So that, to keep high density suppressing such exciton diffu-

sion, an exciton-trapping potential should be implemented for X-BEC. In the previous work [2], authors used a uniaxial stress to form a trapping potential by pressing a bulk crystal with an optical lens. As applied to this way, the uniaxial stress effect is well studied in Cu₂O bulk crystals as reported in [3,4].

On the other hand, we have prepared Cu₂O thin-crystals recrystallized epitaxially in a small gap between paired MgO substrates [5–8]. In such thin-crystals, we have considered that both sample-thinning and formation

Copyright line will be provided by the publisher

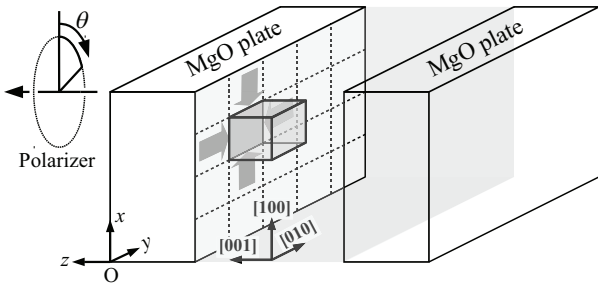


Figure 1 Schematic diagram of Cu_2O thin-crystals sandwiched by paired MgO substrates, where the (001) plane of Cu_2O is grown epitaxially on the (001) surface of the MgO substrate. As a result, a biaxial compressive stress is considered to act on the Cu_2O unit cell as shown thick gray arrows. θ means the polarization angle for detecting PL spectra.

of exciton-trapping potential can be achieved at the same time. A schematic diagram is depicted in Fig. 1, where the (001) plane of Cu_2O is grown epitaxially on the (001) surface of the MgO substrate. Because a lattice constant of Cu_2O ($= 4.27 \text{ \AA}$ [9]) is slightly larger than that of MgO ($= 4.216 \text{ \AA}$ [10]) at room temperature, we can expect that a planar-biaxial compressive stress applies to the Cu_2O unit cell as drawn by thick gray arrows in Fig. 1. In our previous work [7] on the Cu_2O thin-crystal, we took polarizing microscope images and measured complicated photoluminescence (PL) spectra of the 1S yellow ortho-excitons. However, it is difficult to analyze the biaxial stress effect in the Cu_2O thin-crystals because the measured PL spectra complexly consist of weak resonant and intense phonon sideband PL bands due to doubly- or triply-split 1S yellow ortho-exciton states.

In such complicated spectrum analyses, a fitting error function $E(\Theta)$ has many local minima aside from a unique global minimum in a multi-dimensional space for the spectral parameters Θ because the spectral parameters are included nonlinearly in a fitting function $f(x_i; \Theta)$. So that, it is impossible to ensure the statistical correctness of the spectrum analyses in a conventional least-squares method because the solution of spectral parameters will differ depending on searching initial values for Θ due to falling into some local minimum during solution searching. In contrast, the data-driven science has great advantages in the spectral analyses of such complicated spectra. Recently, Nagata *et al.* have applied the Bayesian theorem [11] to spectral deconvolution and have proposed powerful methodology for spectral decomposition [12]. On this methodology, we can stochastically evaluate posterior probability distributions of the spectral parameters with a Markov chain Monte Carlo (MCMC) method [13, 14]. In our previous works [8, 15–17], we have applied the Bayesian inference to the spectral analyses, i.e. Bayesian spectroscopy, in various measured spectra

and have demonstrated the great advantages overcoming constraints in the conventional least-squares method.

In this paper, we measured the polarization dependence of PL spectra owing to the 1S yellow ortho-excitons in the Cu_2O thin-crystal sandwiched by paired MgO substrates. To analyze the change of structural symmetry by the planar-isotropic biaxial stress in Fig. 1, we applied the Bayesian spectroscopy to spectral decomposition, and discussed polarization angle dependences of the resonant PL intensities due to the doubly-split ortho-excitons with considering the symmetry lowering by the biaxial stress.

2 Experimental PL spectra were measured at 4.2 K under weak-excitation conditions by using a cw laser diode of wavelength being 532 nm. To measure the polarization dependence, a polarizer was placed between the sample and a spectrometer, and polarization angles θ were defined as angles from the [100]-direction of the MgO substrate (x -direction) as shown in Fig. 1. The PL was detected from the normal direction of the sample surface. The whole polarization characteristic on photo-detecting sensitivity of the spectrometer and a photo-detector were measured by using a non-polarized mercury lamp, and all PL spectra for the respective θ were calibrated by this polarization characteristic. The thickness of the Cu_2O thin-crystal is ca. $8.5 \mu\text{m}$, which was estimated by the absorption intensity.

3 Bayesian spectroscopy In this section, we explain the methodology of Bayesian spectroscopy [12, 18].

3.1 Bayesian inference Let's consider a regression analysis of a dataset D by a physical model function $f(x_i; \Theta)$. The D is $\{\dots, (x_i, y_i), \dots\}$ and consists of measured PL intensities y_i at photon energy x_i . The data-point number of D is N , and the Θ is a parameter set for the model function $f(x_i; \Theta)$. Since the measured PL intensities $\{y_i\}$ include random noises $\{n_i\}$, the y_i is equivalent with $f(x_i; \Theta) + n_i$, and the mean squared error $E(\Theta)$ is defined by Eq. (1). The conventional least squares method tries to find a solution of Θ by minimizing $E(\Theta)$ with some algorithm such like steepest descent method.

$$E(\Theta) \equiv \frac{1}{2N} \sum_{i=1}^N [y_i - f(x_i; \Theta)]^2. \quad (1)$$

In the data driven science, we deal with a joint probability $P(D, \Theta)$ between a cause Θ and a result D in a causality $\Theta \mapsto D$. According to the causality, the cause Θ has a prior probability $P(\Theta)$, and the result D will be given with a conditional probability $P(D|\Theta)$ under the cause being Θ , and subsequently, the joint probability $P(D, \Theta)$ can be written as $P(D|\Theta)P(\Theta)$. On the basis of the Bayesian theorem [11] for these Θ and D , the $P(D, \Theta)$ can be also expanded to $P(\Theta|D)P(D)$ with a prior probability $P(D)$ for the dataset D and a conditional probability $P(\Theta|D)$ of the cause Θ . The $P(\Theta|D)$ is the posterior probability of Θ after measurement of the dataset D and is what we want to

know. As a result, the $P(\Theta|D)$ is expressed in Eq. (2), and it is found that the $P(\Theta|D)$ is proportional to $P(D|\Theta)$ [12] because the $P(D)$ becomes constant after finishing measurements.

$$P(\Theta|D) = \frac{P(D|\Theta)P(\Theta)}{P(D)} \propto P(D|\Theta)P(\Theta). \quad (2)$$

3.2 Bayes free energy It can be considered that the noises $\{n_i\}$ in the measured data $\{y_i\}$ are Gaussian random noises because thermal random noises coming from dark current are superposed upon signal outputs from photo-detector (photomultiplier tube) and the measured data $\{y_i\}$ were recorded after subtraction of the averaged dark current. However, we have to evaluate a standard deviation σ_{noise} of the Gaussian random noises in order to get $P(D|\Theta)$ in Eq. (2) [18]. In some measurements, it might be difficult to determine σ_{noise} experimentally. In order to solve this problem, Bayesian methodology was proposed to estimate the σ_{noise} only from measured data without any prior informations [18]. In this methodology, quasi-inverse temperatures b are introduced, and the σ_{noise} can be estimated to be $\sigma_{\text{noise}} = \hat{b}^{-1/2}$ by an optimal \hat{b} , which is estimated by minimization of Bayes free energy $F(b)$ as proposed in [18].

Because of the noises $\{n_i\}$ being Gaussian random noises, the conditional probability $P(D|\Theta, b)$ of the dataset D is written in Eq. (3) [18]. At the same time, the conditional probability $P(\Theta|D, b)$ of the parameter set Θ is written in Eq. (4) in the similar way with Eq. (2).

$$P(D|\Theta, b) = \left(\frac{b}{2\pi}\right)^{\frac{N}{2}} \exp[-bNE(\Theta)]. \quad (3)$$

$$P(\Theta|D, b) = \frac{P(D|\Theta, b)P(\Theta|b)}{P(D|b)}. \quad (4)$$

The denominator $P(D|b)$ in Eq. (4) is a normalization factor for the numerator $P(D|\Theta, b)P(\Theta|b)$. Here, we shall consider the correspondence between these formulations and the statistical mechanics. If the Θ and $E(\Theta)$ are considered as a physical state and its energy, respectively, it turns out that the $P(D|\Theta, b)$ in Eq. (3) is equivalent with a Boltzmann factor at a certain inverse temperature b , and the $P(\Theta|b)$ in Eq. (4) is equivalent with a density-of-state for the state Θ . So that, one can understand that the marginalization for $P(D|b)$ in the Θ space is the same with a definition of a partition function $Z(b)$ in statistical mechanics as follows: [18]

$$P(D|b) = \int d\Theta P(D|\Theta, b)P(\Theta|b) \equiv Z(b).$$

Consequently, we can define a Bayes free energy $F(b)$ as $F(b) \equiv -\ln Z(b)$ [18].

The standard deviation σ_{noise} of the Gaussian random noises $\{n_i\}$ can be obtained by estimation of an optimal \hat{b} [18]. The conditional probability $P(b|D)$ of b under D

given is written as $P(D|b)P(b)/P(D)$ by the Bayesian theorem for the causality $b \mapsto D$. Thus, one can understand that this posterior probability $P(b|D)$ is proportional to $Z(b)$ ($= P(D|b)$) because the prior probability $P(b)$ is constant in any b when we do not have any prior informations about the noise intensity. Consequently, the optimal \hat{b} can be estimated by maximization of the $P(b|D)$, and this maximization is equivalent with minimization of the Bayes free energy $F(b)$ as seen in Eq. (5) [18].

$$\hat{b} = \arg \max_b P(b|D) = \arg \min_b F(b). \quad (5)$$

3.3 Replica exchange Monte Carlo method The posterior probability $P(\Theta|D, \hat{b})$ of the parameter set Θ is written in Eq. (6) at the optimal \hat{b} .

$$P(\Theta|D, \hat{b}) \propto \exp[-\hat{b}NE(\Theta)] P(\Theta|\hat{b}). \quad (6)$$

In order to sample $P(\Theta|D, \hat{b})$ effectively in the Θ space, we employed a replica exchange Monte Carlo (RXMC) method [15, 18, 19]. We prepared L replicas with b differing from the high temperature limit $b_1 = 0$ to the sufficiently lower temperature b_L ($\{b_1 < b_2 < \dots < b_\ell < \dots < b_L\}$). In the respective replica of b_ℓ , the parameter set Θ_ℓ was updated and recorded by the Metropolis algorithm [20], and simultaneously, the parameter sets Θ_ℓ and $\Theta_{\ell+1}$ at the nearest neighbor replicas were exchanged stochastically on the basis of the following probability ratio w , where the detailed balance is maintained to get unique and correct $P(\Theta|D, \hat{b})$ [19].

$$w = \min \left(1, \frac{P(\Theta_{\ell+1}|D, b_\ell)P(\Theta_\ell|D, b_{\ell+1})}{P(\Theta_\ell|D, b_\ell)P(\Theta_{\ell+1}|D, b_{\ell+1})} \right).$$

In the series of $\{b_\ell\}$, the respective b_ℓ were given by a geometrical progression, and the b_2 and b_L were selected to be sufficiently wide as \hat{b} being $b_2 \ll \hat{b} \ll b_L$ [15].

The Bayes free energy $F(b_\ell)$ in Sec. 3.2 can be obtained in the following relation [18]:

$$F(b_\ell) = b_\ell \tilde{F}(b_\ell) - \frac{N}{2} (\ln b_\ell - \ln 2\pi). \quad (7)$$

In Eq. (7), the quasi-free energy $\tilde{F}(b_\ell)$ is also defined as $-(1/b_\ell) \ln \tilde{Z}(b_\ell)$, which $\tilde{Z}(b_\ell) \equiv (2\pi/b_\ell)^{N/2} Z(b_\ell)$, and is calculated as Eq. (8) [12, 18].

$$\begin{aligned} \tilde{F}(b_\ell) &= -\frac{1}{b_\ell} \ln \prod_{\ell'=1}^{\ell-1} \frac{\tilde{Z}(b_{\ell'+1})}{\tilde{Z}(b_{\ell'})} \\ &= -\frac{1}{b_\ell} \sum_{\ell'=1}^{\ell-1} \ln \left\langle e^{-N(b_{\ell'+1}-b_{\ell'})E(\Theta_{\ell'})} \right\rangle_{b_{\ell'}}. \end{aligned} \quad (8)$$

From Eqs. (7) and (8), we can evaluate the Bayes free energy using $E(\Theta_{\ell'})$ in each replica.

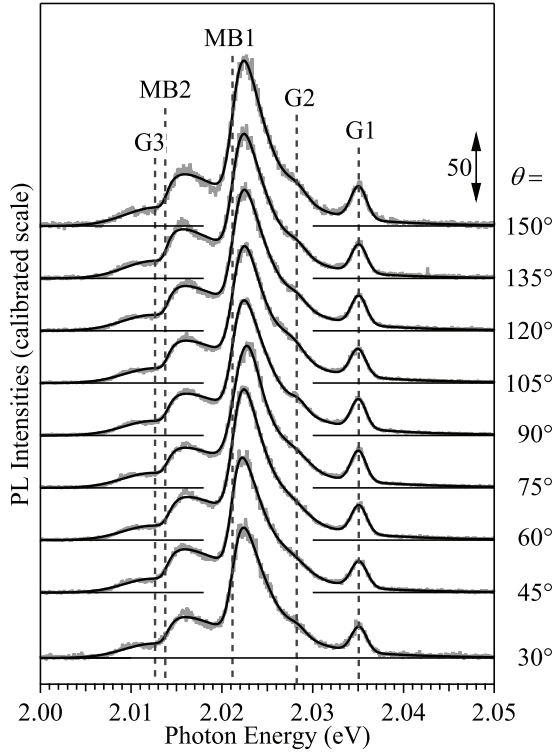


Figure 2 Polarization dependence of PL spectra in a Cu_2O thin-crystal sandwiched by paired MgO substrates. Gray and black lines are measured and reproduced spectra, respectively. Vertical broken lines mean transition and threshold transition energies of the spectral components of G1~G3 and MB1~MB2, respectively. A vertical double-head arrow denotes the scale of calibrated PL intensity.

4 Results Gray lines in Fig. 2 show the PL spectra detected at the respective polarization angles θ . These PL spectra include five spectral components G1, G2, MB1, MB2, and G3 in order from higher to lower energy sides. The intense PL bands MB1 and MB2 have tails on higher energy side, and their Stokes shifts from the spectral components G1 and G2 are equal to ca. 14 meV, where this value is identical with the energy of Γ_{12}^- phonon in Cu_2O [7,21]. Therefore, one can conclude that the G1 and G2 are resonant PL bands due to doubly-split 1S yellow ortho-exciton states, and the MB1 and MB2 are their phonon sideband PL by the Γ_{12}^- phonon [7]. At this moment, the origin of G3 band is unknown.

By simple consideration of symmetry lowering, we can explain that the energy splitting of the resonant PL bands G1 and G2 comes from the planar-isotropic biaxial stress in Fig. 1. As summarized in Table 1(a), a stress-free crystal of Cu_2O has a cubic symmetry O_h , and the 1S yellow ortho-exciton states $^3\Gamma_5^+$ degenerate triply [3]. In contrast, the structural symmetry degrades to tetragonal one in the Cu_2O thin-crystal as shown in Table 1(b) because the

planar-isotropic biaxial stress acts on unit cells in [100] and [010] directions as shown in Fig. 1, and subsequently, an anisotropy in z direction emerges. Consequently, the ortho-exciton states split into anisotropic and two isotropic ones as seen in Table 1(b).

Focusing on the difference in PL intensities between G1 and G2, the difference cannot be explained by the difference in the degree of degeneracy between the doubly-split ortho-exciton states (1:2). As seen in Fig. 2, the PL intensity of G1 is much stronger than that of G2. Thus, we have to consider selection rules on the optical transitions of these resonant PL bands. In addition, we will explain the polarization dependences of these resonant PL intensities by symmetry lowering. As seen in Fig. 2, although polarization dependency cannot be recognized in the strong spectral components G1, MB1, MB2 and G3, the weak shoulder component G2 seems to exhibit a polarization dependency. To discuss such difference, we will apply the Bayesian spectroscopy for spectral decomposition.

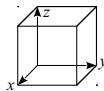
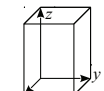
5 Discussion In this section, we discuss the polarization dependences of the resonant PL intensities due to doubly-split 1S yellow ortho-exciton states on the basis of Table 1, in which the complicated PL spectra are decomposed by the Bayesian spectroscopy with appropriate spectral line-shape functions.

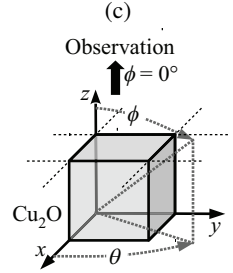
5.1 Optical selection rules and their polarization dependences In stress-free Cu_2O crystals, basis functions of the ortho-exciton states $^3\Gamma_5^+$ have radial characteristics of xy , yz and zx [3,22] as shown in Table 1(a), and these characteristics are equivalent with each other in the cubic symmetry. In contrast, such isotropic nature is collapsed by the planar-isotropic biaxial stress depicted in Fig. 1. As a result, the exciton state $^1\Gamma_4^+$ having a radial characteristic of xy deviates from the double-fold exciton states $^2\Gamma_5^+$ as seen in Table 1(b), where the exciton states $^2\Gamma_5^+$ have radial characteristics of yz and zx .

The resonant PL due to the ortho-exciton states brings about by quadrupole transitions [3,7]. The quadrupole-transition operator can be expressed as $xy \sin \phi \sin \theta + yz \cos \phi \sin \theta + zx \cos \theta$ [3] by using radial characteristics (xy , yz and zx) and angles ϕ and θ , where the ϕ and θ are depicted in Table 1(c), and specify the propagating direction and polarization angles of PL photons, respectively. So that, in the case of stress-free Cu_2O crystals, a quadrupole-transition matrix element $M_{O_h} (\equiv \langle ^1\Gamma_1^+ | ^3\Gamma_5^+ | ^3\Gamma_5^+ \rangle)$ between the ortho-exciton $^3\Gamma_5^+$ and the ground state $^1\Gamma_1^+$ has three terms in Eq. (9).

$$M_{O_h} = \begin{cases} \iiint (xy \sin \phi \sin \theta) xy \, dx dy dz & \propto \sin \phi \sin \theta, \\ \iiint (yz \cos \phi \sin \theta) yz \, dx dy dz & \propto \cos \phi \sin \theta, \\ \iiint (zx \cos \theta) zx \, dx dy dz & \propto \cos \theta. \end{cases} \quad (9)$$

Table 1 Summary of structural symmetries and the 1S yellow ortho-exciton states: (a) stress-free crystal, (b) thin-crystal sandwiched MgO substrates. (c) configuration of ϕ and polarization angle θ .

	Unit cell	Stress directions	Symmetry (Symbol)	1S yellow ortho-exciton		
				Levels	Symmetry notation	Basis function characteristic
(a) Stress-free		—	Cubic (O_h)	\equiv	${}^3\Gamma_5^+$	$\begin{cases} xy \\ yz \\ zx \end{cases}$
(b) Cu ₂ O (001) on MgO (001)		[100], [010]	Tetragonal (D_{4h})	\equiv	${}^2\Gamma_5^+$	$\begin{cases} yz \\ zx \end{cases}$
				—	${}^1\Gamma_4^+$	$\begin{cases} xy \end{cases}$



As a result, it is found that the $|M_{O_h}|^2$ is independent on the polarization angle θ because the PL photons were detected on the normal direction of the sample surface, i.e. $\phi \approx 0^\circ$, and $\sin^2 \theta + \cos^2 \theta = 1$.

On the other hand, the crystal symmetry is changed to a tetragonal one by the planar-isotropic biaxial stress in the Cu₂O thin-crystals, and the z -axis becomes an anisotropic axis as seen in Table 1. So that, we have to consider different quadrupole-transition matrix elements $M_{D_{4h},xy}$ and $M_{D_{4h},z}$ for the doubly-split exciton states ${}^1\Gamma_4^+$ and ${}^2\Gamma_5^+$, respectively. The transition operators for $M_{D_{4h},xy}$ and $M_{D_{4h},z}$ can be written as $xy \sin \phi \sin \theta$ and $yz \cos \phi \sin \theta + zx \cos \theta$, and they have ${}^1\Gamma_4^+$ and ${}^2\Gamma_5^+$ symmetries, respectively. As a result, polarization dependences are derived in Eqs. (10) and (11) for $M_{D_{4h},xy}$ and $M_{D_{4h},z}$, respectively, and we can discuss the transition strengths by $|M_{D_{4h},xy}|^2$ and $|M_{D_{4h},z}|^2$.

$$M_{D_{4h},xy} \equiv \langle {}^1\Gamma_4^+ | {}^1\Gamma_4^+ | {}^1\Gamma_4^+ \rangle \propto \sin \phi \sin \theta, \quad (10)$$

$$M_{D_{4h},z} \equiv \langle {}^1\Gamma_4^+ | {}^2\Gamma_5^+ | {}^2\Gamma_5^+ \rangle \propto \begin{cases} \cos \phi \sin \theta, \\ \cos \theta. \end{cases} \quad (11)$$

Based on Eq. (11), it is found that the $|M_{D_{4h},z}|^2$ for the ${}^2\Gamma_5^+$ exciton states is independent on θ as written in Eq. (12) because $\cos \phi \sin \theta$ can be approximated to $\sin \theta$ under our detecting configuration of $\phi \approx 0^\circ$ as shown in Fig. 1.

$$|M_{D_{4h},z}|^2 \propto \sin^2 \theta + \cos^2 \theta = 1. \quad (12)$$

This interpretation is consistent with the result that the G1-PL does not show significant polarization dependence as seen in Fig. 2.

In contrast, the G2-PL is much weaker than G1-PL as seen in Fig. 2, and its intensity seems to vary on θ as described in Sec. 4. This result can be also explained in a similar way with considering the quadrupole-transition matrix element $M_{D_{4h},xy}$ for the ${}^1\Gamma_4^+$ exciton state. The polarization dependence is derived as $|M_{D_{4h},xy}|^2 \propto \sin^2 \phi \sin^2 \theta$ from Eq. (10). When the detecting direction angle ϕ is strictly zero, the $|M_{D_{4h},xy}|^2$ becomes zero, and the G2-PL due to the ${}^1\Gamma_4^+$ exciton state becomes quadrupole-forbidden. However, the $\phi = 0^\circ$ restriction is relaxed

since PL photons were detected by a lens with a finite solid angle. As a result, the polarization dependence of $|M_{D_{4h},xy}|^2$ is written as Eq. (13).

$$|M_{D_{4h},xy}|^2 \propto \sin^2 \theta. \quad (13)$$

We would like to discuss the polarization dependences of the G1- and G2-PL intensities by Eqs. (12) and (13). However, the G2-PL is rather weak and lies on the high energy tail of the intense MB1 band as seen in Fig. 1. So that, we should employ the Bayesian spectroscopy for the spectral decomposition.

5.2 Spectral components and the physical model

To reproduce the measured PL spectra, we consider a physical model $f(E; \Theta)$ including five spectral components as written in Eq. (14).

$$f(E; \Theta) = f_{G1} + f_{MB1} + f_{G2} + f_{MB2} + f_{G3}, \quad (14)$$

where E is photon energy and the parameter set Θ consists of the parameter sets $\{\Theta_{G1}, \Theta_{MB1}, \Theta_{G2}, \Theta_{MB2}, \Theta_{G3}\}$ for the respective spectral components.

For the G1- and G2-PL, a normalized Gaussian line-shape function $g(E; E_0, W)$ in Eq. (15) was used.

$$g(E; E_0, W) \equiv \sqrt{\frac{4 \ln 2}{\pi W^2}} \exp\left[-4 \ln 2 \frac{(E - E_0)^2}{W^2}\right], \quad (15)$$

where E_0 and W are a transition energy and a spectral width in full-width at half maximum, respectively. By using $g(E; E_0, W)$ and integrated PL intensities I_{Gn} , the spectral profiles f_{Gn} for the resonant Gn -PL ($n = 1, 2$) are defined as follows:

$$f_{Gn}(E; \Theta_{Gn}) \equiv I_{Gn} \times g(E; E_{Gn}, W_{Gn}).$$

For the phonon sideband PL (MB n ; $n = 1, 2$), we should use a Maxwell-Boltzmann line-shape function $h(E; E_0, T)$ in Eq. (16).

$$h(E; E_0, T) \equiv \sqrt{E - E_0} \exp\left(-\frac{E - E_0}{k_B T}\right), \quad (16)$$

only for $E \geq E_0$,

where E_0 and T are a threshold energy and an effective temperature of thermally-distributed excitons. However, we have to consider spectral broadenings. So, a spectral function $f_{\text{MB}n}$ ($n = 1, 2$) for the MB n -PL was defined as Eq. (17).

$$f_{\text{MB}n}(E; \Theta_{\text{MB}n}) \equiv I_{\text{MB}n} \times \int h(E + \varepsilon; E_{\text{MB}n}, T_{\text{MB}n}) g(\varepsilon; W_{\text{MB}n}) d\varepsilon, \quad (17)$$

where $I_{\text{MB}n}$ means PL intensity, and the spectral broadenings are taken into account with $W_{\text{MB}n}$ and a normalized Gaussian distribution of the same function with Eq. (15).

5.3 Bayesian spectroscopy In the $f(E; \Theta)$, we have 17 parameters in Θ . Such multivariate analyses should be performed with the RXMC method. We prepared 40 replicas ($L = 40$), the quasi-inverse temperatures b_2 and b_{40} were set to be 1.2×10^{-3} and 5.0, and they correspond to 2.9×10^1 and 4.5×10^{-1} in the PL intensity scale, respectively. As confirmed in Fig. 2, it is found that the required condition of $b_2 \ll \hat{b} \ll b_{40}$ is well satisfied. The posterior probabilities $P(\Theta|D, \hat{b})$ were sampled through Monte Carlo iterations of 50,000 steps after sufficient burn-in phase (50,000 steps).

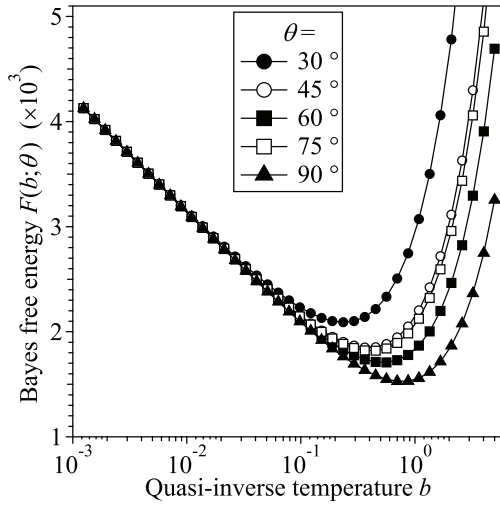


Figure 3 Bayes free energies $F(b)$ as functions of quasi-inverse temperature b .

5.3.1 Bayes free energy Figure 3 shows the Bayes free energies $F(b)$ as functions of quasi-inverse temperature b , where the abscissa for b is in logarithmic scale. As seen in Fig. 3, these $F(b)$ have minimum values at the optimal $\hat{b}(\theta)$ as expressed in Eq. (5), and it is found that the $\hat{b}(\theta)$ tends to increase as θ increases ($\theta \leq 90^\circ$). The variation of $\hat{b}(\theta)$ corresponds to the noise intensity variation, and this tendency means that the σ_{noise} becomes small at $\theta \sim 90^\circ$. Since the PL intensities in Fig. 2 are displayed on the calibrated scale with θ -dependent photo-detecting sensitivity, this variation of σ_{noise} is reasonable, in which the

photo-detecting sensitivity drops as the polarization angles θ departs from 90° .

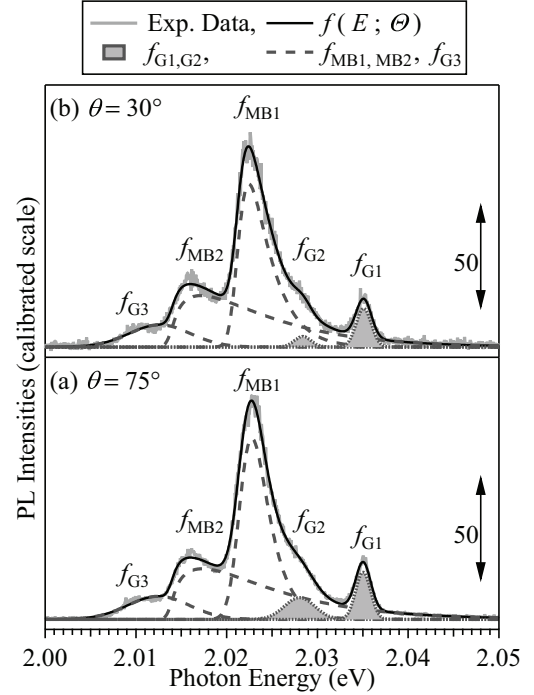


Figure 4 Typical results for spectral reproduction by Bayesian spectroscopy at (a) 75° and (b) 30° . Gray and black lines are measured and reproduced PL spectra, respectively. Dashed and dotted lines denote the respective spectral components in the reproduced ones.

5.3.2 Spectral decomposition Figure 4 shows typical results for spectral reproduction by Bayesian spectroscopy, where (a) and (b) are for $\theta = 75^\circ$ and 30° , respectively. Gray and black solid lines are measured and reproduced PL spectra, respectively, and dashed and dotted lines denote the respective spectral components in the reproduced ones. In these spectra, mean values $\hat{\Theta}$ are used for the parameter set Θ . The mean values $\hat{\Theta}$ were obtained from samplings after burn-in phase. As seen in Fig. 4, the physical model $f(E; \hat{\Theta})$ can reproduce well the measured PL spectra. Here, we should note intensity difference between the resonant G1- and G2-PL, which are depicted by gray areas in Fig. 4. It is found that the G1-PL intensity hardly change, whereas the G2-PL intensity decreases at $\theta = 30^\circ$ as seen in Fig. 4(b).

Table 2 is the result of the Bayesian spectroscopy on all PL spectra in Fig. 2, in which estimated values are shown with a format of $\hat{\Theta} \pm \sigma_\Theta$ with the mean values $\hat{\Theta}$ and the standard deviations σ_Θ of their posterior probability distributions $P(\Theta|D, \hat{b})$. The optimal quasi-inverse temperature \hat{b} and the corresponding noise intensities are also listed in Table 2(a), where the noise intensities are

Table 2 Mean values $\hat{\Theta}$ of the parameter set and standard deviations σ_{Θ} of their posterior probability distributions $P(\Theta|D, \hat{b})$: (a) for the resonant PL bands f_{G1} and f_{G2} , (b) for the phonon sideband PL bands f_{MB1} and f_{MB2} . The optimal quasi-inverse temperature \hat{b} and the corresponding noise intensities σ_{noise} are also listed in (a).

(a) f_{G1}, f_{G2}								
θ ($^{\circ}$)	f_{G1}			f_{G2}			\hat{b}	σ_{noise}
	\hat{E}_{G1} (meV)	\hat{I}_{G1} $\times 10^{-3}$	\hat{W}_{G1} (meV)	\hat{E}_{G2} (meV)	\hat{I}_{G2} $\times 10^{-3}$	\hat{W}_{G2} (meV)		
30	2035.10 \pm 0.02	40.0 \pm 0.8	1.97 \pm 0.06	2028.38 \pm 0.16	12.0 \pm 0.9	2.16 \pm 0.53	0.24	2.1
45	2035.10 \pm 0.02	43.4 \pm 0.7	2.08 \pm 0.04	2028.01 \pm 0.08	22.9 \pm 1.6	3.51 \pm 0.20	0.36	1.7
60	2035.10 \pm 0.01	45.6 \pm 0.6	2.00 \pm 0.03	2028.00 \pm 0.06	26.7 \pm 1.1	3.69 \pm 0.14	0.56	1.3
75	2035.04 \pm 0.01	48.1 \pm 0.7	1.94 \pm 0.03	2028.03 \pm 0.05	44.7 \pm 1.7	3.91 \pm 0.11	0.45	1.5
90	2035.05 \pm 0.01	45.8 \pm 0.5	1.94 \pm 0.03	2028.49 \pm 0.04	13.1 \pm 0.6	2.01 \pm 0.11	0.70	1.2
105	2034.99 \pm 0.01	45.3 \pm 0.6	2.05 \pm 0.03	2027.82 \pm 0.03	34.8 \pm 1.0	3.11 \pm 0.07	0.56	1.3
120	2035.08 \pm 0.01	45.6 \pm 0.6	1.97 \pm 0.03	2028.35 \pm 0.06	14.5 \pm 0.8	2.36 \pm 0.13	0.45	1.5
135	2035.10 \pm 0.02	45.5 \pm 0.8	1.99 \pm 0.04	2028.34 \pm 0.08	16.8 \pm 1.1	2.49 \pm 0.52	0.24	2.1
150	2035.06 \pm 0.02	54.2 \pm 1.0	2.06 \pm 0.05	2028.36 \pm 0.08	20.9 \pm 1.3	2.52 \pm 0.16	0.15	2.6
$\langle \hat{\Theta} \rangle$	2035.07 \pm 0.01		2.00 \pm 0.02	2028.20 \pm 0.07		2.86 \pm 0.22		

(b) f_{MB1}, f_{MB2}								
θ ($^{\circ}$)	f_{MB1}				f_{MB2}			
	\hat{E}_{MB1} (meV)	\hat{I}_{MB1} $\times 10^{-3}$	\hat{T}_{MB1} (K)	\hat{W}_{MB1} (meV)	\hat{E}_{MB2} (meV)	\hat{I}_{MB2} $\times 10^{-3}$	\hat{T}_{MB2} (K)	\hat{W}_{MB2} (meV)
30	2020.990 \pm 0.008	382 \pm 2	23.3 \pm 0.1	1.70 \pm 0.02	2013.74 \pm 0.03	353 \pm 3	77.3 \pm 0.6	1.21 \pm 0.09
45	2020.900 \pm 0.007	388 \pm 2	23.3 \pm 0.2	1.53 \pm 0.02	2013.70 \pm 0.02	356 \pm 2	71.1 \pm 0.5	1.19 \pm 0.07
60	2021.030 \pm 0.005	430 \pm 1	21.6 \pm 0.1	1.83 \pm 0.01	2013.89 \pm 0.02	390 \pm 2	77.6 \pm 0.4	1.30 \pm 0.06
75	2021.360 \pm 0.008	392 \pm 2	17.6 \pm 0.2	2.36 \pm 0.02	2013.72 \pm 0.02	366 \pm 2	81.8 \pm 0.5	1.10 \pm 0.07
90	2021.010 \pm 0.005	399 \pm 1	23.3 \pm 0.1	1.80 \pm 0.01	2013.77 \pm 0.02	383 \pm 2	80.6 \pm 0.4	1.14 \pm 0.06
105	2021.080 \pm 0.006	388 \pm 1	21.4 \pm 0.1	1.91 \pm 0.02	2013.78 \pm 0.02	379 \pm 2	79.7 \pm 0.5	1.06 \pm 0.06
120	2021.040 \pm 0.005	416 \pm 1	23.1 \pm 0.1	1.77 \pm 0.02	2013.78 \pm 0.02	380 \pm 2	75.3 \pm 0.5	1.08 \pm 0.06
135	2021.000 \pm 0.007	430 \pm 2	23.2 \pm 0.1	1.77 \pm 0.02	2013.68 \pm 0.02	382 \pm 3	70.8 \pm 0.7	0.97 \pm 0.07
150	2021.000 \pm 0.007	488 \pm 2	22.5 \pm 0.1	1.83 \pm 0.02	2013.70 \pm 0.01	420 \pm 3	76.1 \pm 0.3	1.02 \pm 0.04
$\langle \hat{\Theta} \rangle$	2021.046 \pm 0.040		22.1 \pm 0.6	1.83 \pm 0.07	2013.75 \pm 0.02		76.7 \pm 1.2	1.12 \pm 0.03

indicated by the standard deviations $\sigma_{\text{noise}} (= \hat{b}^{-1/2})$ of the Gaussian random noises. Through careful checking of Table 2, it is found that the parameters other than the PL intensities hardly change with θ . The bottom lines in Tables 2(a) and (b) show the mean values $\langle \hat{\Theta} \rangle$ obtained from the $\hat{\Theta}$ at the respective θ and their standard deviation $\sigma_{\langle \hat{\Theta} \rangle}$. These $\sigma_{\langle \hat{\Theta} \rangle}$ are sufficiently small, and it is guaranteed that the spectral parameters other than the PL intensities have no polarization dependence. In addition, a phonon energy providing the phonon sideband PL was also estimated to be 14.12 ± 0.04 meV from the energy difference between \hat{E}_{Gn} and \hat{E}_{MBn} ($n = 1, 2$), and it is consistent with the previous results [7, 21].

5.3.3 Polarization dependences of \hat{I}_{G1} and \hat{I}_{G2}

Figure 5 shows polarization dependences of the resonant G1- and G2-PL intensities of the doubly-split ortho-exciton states, where closed and open circles denote the

\hat{I}_{G1} and \hat{I}_{G2} , respectively, and error bars mean the standard deviations of the posterior probability distributions $P(I_{Gn}|D, \hat{b})$ ($n = 1, 2$). As clearly seen in Fig. 5, the polarization dependence of \hat{I}_{G1} is not so obvious, and it is well explained by a solid semi-circle in Fig. 5, which was drawn on the basis of the $|M_{D_{4h,z}}|^2$ in Eq. (12) for the ${}^2\Gamma_5^+$ ortho-exciton states.

In contrast, the \hat{I}_{G2} seems to exhibit polarization dependence in Fig. 5. Although the open circles for \hat{I}_{G2} are slightly scattered, it is recognized that the \hat{I}_{G2} tends to increase at $\theta = 60^{\circ} \sim 120^{\circ}$. As discussed in Sec. 5.1, the ${}^1\Gamma_4^+$ ortho-exciton state is expected to indicate a polarization dependence of $\sin^2 \theta$ as seen in $|M_{D_{4h,xy}}|^2$ of Eq. (13). The polarization dependence of $|M_{D_{4h,xy}}|^2$ is drawn by a gray curve in Fig. 5, and it explains the tendency of the \hat{I}_{G1} to increase at $\theta = 60^{\circ} \sim 120^{\circ}$.

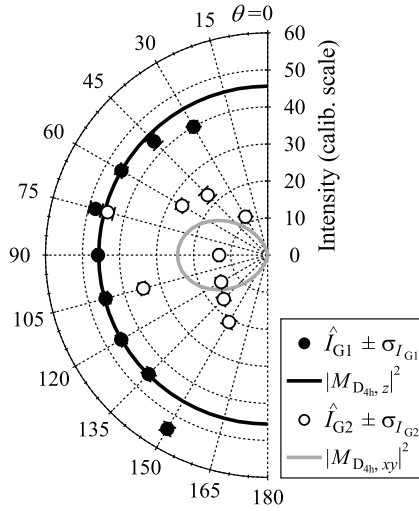


Figure 5 Polarization dependences of the resonant PL intensities of the doubly-split ortho-exciton states. Closed and open circles are for \hat{I}_{G1} and \hat{I}_{G2} , respectively. Error bars mean the standard deviations of their posterior probability distributions. Black and gray lines display polarization dependences of $|M_{D_{4h},z}|^2$ and $|M_{D_{4h},xy}|^2$, respectively.

These agreements on the \hat{I}_{G1} and \hat{I}_{G2} mean that our interpretation proposed in Sec. 5.1 are consistent with the experimental results. So that, it is confirmed that, owing to a small lattice mismatch, the planar-isotropic biaxial stress is introduced to the Cu_2O thin-crystals sandwiched paired MgO substrates, and such biaxial stress degrades the crystal symmetry to D_{4h} from O_h as summarized in Table 1.

As described in Sec. 5.1, the $|M_{D_{4h},xy}|^2$ becomes zero when the detecting direction angle ϕ is strictly zero. Therefore, finally, we would like to discuss the forbidden degree on the resonant G2-PL. As seen in Eqs. (10) and (11), the $|M_{D_{4h},xy}|^2$ and $|M_{D_{4h},z}|^2$ are found to be proportional to $\sin^2 \phi$ and $\cos^2 \phi$ at $\theta = 90^\circ$, respectively. In our experimental setup, the detecting solid angle corresponds to $\phi = -14^\circ \sim +14^\circ$, and the ratio $|M_{D_{4h},xy}|^2/|M_{D_{4h},z}|^2$ is estimated to be approximately 2.0×10^{-2} , which was obtained from ϕ integral. However, in Fig. 5, we found that the ratio of the resonant PL intensities ($\hat{I}_{G2}/\hat{I}_{G1}$) is larger than that small ratio. It is well known that other extrinsic factors such like sample inhomogeneity and point defects frequently causes such alleviation of forbidden transition, and such extrinsic factors might enhance the G2-PL. Even so, the conclusion described in the immediately preceding paragraph is well maintained.

6 Summary We measured the polarization dependence of the PL spectra in a Cu_2O thin-crystal sandwiched by paired MgO substrates and investigated their polarization dependences on the basis of symmetry degradation induced by the planar-isotropic biaxial stress owing to

a small lattice mismatch between Cu_2O and MgO. To quantify this research, we introduced the Bayesian spectroscopy to decompose the complicated spectra and to get posterior probability distributions of the spectral parameters in the respective spectral components. Although the resonant and the phonon sideband PL bands due to the doubly-split ortho-exciton states co-exist with overlapping each other, we succeeded in decomposing these spectral components. From these quantitative analyses, different polarization dependences were found on the PL intensities between the doubly-split resonant G1- and G2-PL. The G1-PL appearing on high energy side does not show significant dependency. In contrast, the G2-PL intensity exhibits the tendency to increase at $\theta = 60^\circ \sim 120^\circ$.

By the planar-isotropic biaxial stress in Cu_2O thin-crystals, the crystal symmetry degrades to the tetragonal symmetry from the cubic one. Owing to such lowering of the crystal symmetry, the ortho-exciton state splits into the doubly-split exciton states: ${}^2\Gamma_5^+$ and ${}^1\Gamma_4^+$. We considered the optical selection rules and their polarization dependences on the basis of the quadrupole-optical transition and the radial characteristics of the basis functions for the respective exciton states. As a result, it is found that, in the ${}^2\Gamma_5^+$ exciton state, the quadrupole-transition is allowed and it does not exhibit significant polarization dependence. In contrast, although the optical transition of the ${}^1\Gamma_4^+$ exciton state is quadrupole-forbidden at the restrict condition of $\phi = 0^\circ$, such quadrupole-forbidden is considered to be relaxed by detecting setup for the PL spectra with finite solid angle of $\phi = -14^\circ \sim +14^\circ$, and the transition strength of the ${}^1\Gamma_4^+$ exciton state is considered to vary with $\sin^2 \theta$. Both polarization dependences for the ${}^2\Gamma_5^+$ and ${}^1\Gamma_4^+$ exciton states can explain the polarization dependences of the G1- and G2-PL intensities. Consequently, it is concluded that the planar-isotropic biaxial stress owing to a small lattice mismatch degrades the crystal symmetry to D_{4h} , and divide the ortho-exciton state into doubly-split exciton states indicating different polarization dependences.

Acknowledgment This work was supported by JSPS KAKENHI Grant Numbers 16H01552, 16H04002, and 16K13824.

References

- [1] D. Snoko and G.M. Kavoulakis, Rep. Prog. Phys. **77**, 116501 (2014).
- [2] K. Yoshioka, E. Chae, and M. Kuwata-Gonokami, Nat. Commun. **2**, 328 (2011).
- [3] H.R. Trebin, H.Z. Cummins, and J.L. Birman, Phys. Rev. B **23**, 597 (1981).
- [4] A. Mysyrowicz, D.P. Trauernicht, J.P. Wolfe, and H.R. Trebin, Phys. Rev. B **27**, 2562 (1983).
- [5] K. Iwamitsu, S. Aihara, T. Shimamoto, A. Fujii, and I. Akai, Eur. Phys. J. B **86**, 194 (2013).
- [6] K. Iwamitsu, S. Aihara, A. Ota, F. Ichikawa, T. Shimamoto, and I. Akai, J. Phys. Soc. Jpn. **83**, 124714 (2014).

- [7] S. Aihara, A. Ota, K. Iwamitsu, F. Ichikawa, H. Isobe, T. Shimamoto, and I. Akai, *J. Lumin.* **167**, 211 (2015).
- [8] K. Iwamitsu, S. Aihara, M. Okada, and I. Akai, *J. Phys. Soc. Jpn.* **85**, 094716 (2016).
- [9] A. Werner and H. D. Hochheimer, *Phys. Rev. B* **25**, 5929 (1982).
- [10] K. Hirata, K. Moriya, and Y. Waseda, *J. Mater. Sci.* **12**, 838 (1977).
- [11] T. Bayes and R. Price, *Phil. Trans. Roy. Soc.* **53**, 370 (1763).
- [12] K. Nagata, S. Sugita, and M. Okada, *Neural Netw.* **28**, 82 (2012).
- [13] P. J. Green, *Biometrika* **82**, 711 (1995).
- [14] C. Andrieu, N. D. Freitas, A. Doucet, and M. I. Jordan, *Machine Learning* **50**, 5 (2003).
- [15] K. Iwamitsu, Y. Furukawa, M. Nakayama, M. Okada, and I. Akai, *J. Lumin.* **197**, 18 (2018).
- [16] S. Aihara, M. Hamamoto, K. Iwamitsu, M. Okada, and I. Akai, *AIP Adv.* **7**, 045107 (2017).
- [17] I. Akai, K. Iwamitsu, and M. Okada, *J. Phys.: Conf. Ser.* *in press* (2018).
- [18] S. Tokuda, K. Nagata, and M. Okada, *J. Phys. Soc. Jpn.* **86**, 024001 (2017).
- [19] K. Hukushima and K. Nemoto, *J. Phys. Soc. Jpn.* **65**, 1604 (1996).
- [20] N. Metropolis, A. W. Rosenbluth, M. N. Rosenbluth, A. H. Teller, and E. Teller, *J. Chem. Phys.* **21**, 1087 (1953).
- [21] R. G. Waters, F. H. Pollak, R. H. Bruce, and H. Z. Cummins, *Phys. Rev. B* **21**, 1665 (1980).
- [22] R. J. Elliott, *Phys. Rev.* **124**, 340 (1961).